RSC Advances

PAPER

View Article Online
View Journal | View Issue

Cite this: *RSC Adv.*, 2024, **14**, 29160

Atomic-scale description of 2D Janus MoSO and MoSeO formation: oxidation patterns and band-gap engineering†

Jair Othoniel Dominguez Godinez,[a] Héctor Noé Fernández Escamilla,[b] José de Jesús Quijano Briones,[b] José Israel Paez Ornelas,[c] Eduardo Peréz Tijerina,[b] R. Ponce-Pérez,[c] D. M. Hoat*[de] and Jonathan Guerrero Sánchez[c]

Transition metal dichalcogenides (TMDs) have attracted attention due to their broad-ranging physical properties. Their semiconducting characteristics make them attractive for nanotechnology applications. In particular, molybdenum disulfide (MoS_2) and molybdenum diselenide ($MoSe_2$) possess direct band gaps of 1.62 and 1.45 eV, respectively. Both monolayers are prone to oxidation in oxygen-rich environments. In this sense, we have studied the oxidation process in these 2D systems using first-principles calculations based on density functional theory. The stability of several oxidized structures under different growth conditions was analyzed *via* a formation-energy study, where the Janus oxidized phases are stable in oxygen-rich environments. The oxidation process is not random. Instead, it has a well-defined pattern, forming diagonal structures before reaching a complete monolayer. We have observed a systematic band-gap reduction as oxygen content increases, reaching 1.12 eV for MoSO and 0.83 eV for MoSeO, and a direct-to-indirect band-gap transition occurs at the early stages of oxidation. Our study is a step further towards designing new monolayers with engineered electronic properties and increasing reactivity towards molecules with a positive polarity on the O side of the monolayers.

Received 19th April 2024
Accepted 19th July 2024

DOI: 10.1039/d4ra02928c

rsc.li/rsc-advances

1 Introduction

Since the discovery of graphene in 2004,[1] the paradigm of two-dimensional materials has emerged and is still relevant. There are several families among the 2D nanomaterials, such as graphene-like 2D semiconductors (silicene, germanene, stanene, and phosphorene), MXenes, MOenes, and transition metal dichalcogenides (TMDs), among others.[2] The TMD family is of great importance. These materials are formed by a layer of transition metal atoms sandwiched between two chalcogen layers. Their chemical formula is MX_2, where M is a transition metal atom, and X is a chalcogen atom.[3] In this family, MoS_2 and $MoSe_2$ are among the most important members. They possess semiconductor characteristics,[4] so they can be used for applications in nanoelectronics, for example, in logic devices such as field-effect transistors (FETs).[5–7] When MoS_2 and $MoSe_2$ are exposed to an oxygen-rich environment, spontaneous oxidation occurs mainly in the sulfur and selenium vacancies – common defects in these materials – and affects their electronic and structural properties.[8]

Furthermore, TMD engineering to form the so-called Janus family is of great importance since it induces an extra degree of freedom: the electronic asymmetry that is finding several new applications in catalysis because it promotes deformations that may induce higher activities.[9] It also presents a vertical electric field, induced due to the lack of mirror symmetry,[10] which induces a different contact potential in the TMD/Janus TMD heterojunctions.[10] For example, Janus $MoSO/MoS_2$ is a type-II semiconductor with an exciton binding energy of 0.07 eV, which facilitates electron–hole separation for applications in nanodevices.[10] The Janus MoSSe monolayer can be obtained *via* selenization applied to the MoS_2 monolayer.[11] In this process, one of the S layers is removed by H_2 plasma to form MoSH, with further selenization to MoSSe by thermal decomposition of Se powders.[11]

Similarly, a TMD can be oxidized to obtain Janus monolayers. For example, substituting selenium or sulfur with oxygen atoms affects the structural and electronic properties of the treated monolayers. In its pristine structure, MoS_2 has a direct band gap that changes to indirect for MoSO.[12] Also, when oxidizing MoS_2 at high temperatures, O_2 reacts with the

[a]*Centro de Investigación Científica y de Educación Superior de Ensenada, Zona Playitas, Ensenada, 22860, Baja Califonia, Mexico*
[b]*Centro de Investigación en Ciencias Físico Matemáticas, Universidad Autónoma de Nuevo León, Ciudad Universitaria, San Nicolás, 66451, Nuevo León, Mexico*
[c]*Centro de Nanociencias y Nanotecnología Ensenada, B.C., ZonaPlayitas, Ensenada, 22860, Baja Califonia, Mexico*
[d]*Institute of Theoretical and Applied Research, Duy Tan University, Ha Noi, 100000, Vietnam. E-mail: dominhhoat@duytan.edu.vn*
[e]*Faculty of Natural Sciences, Duy Tan University, Da Nang, 550000, Vietnam*

† Electronic supplementary information (ESI) available. See DOI: https://doi.org/10.1039/d4ra02928c

monolayer's surface, degrading the mechanical properties.[13] So far, modifying Se- and S-based TMDs to obtain their Janus counterparts (MoSO and MoSeO) has been of great interest due to the new applications that such monolayers may find in optoelectronic devices,[14] along with photocatalytic properties for solar cell applications.[15] Additionally, MoSO shows strong out-of-plane piezoelectricity.[12] Considering the previous discussion and since the transition from a TMD to Janus TMD is not expected to be abrupt,[8] we are interested in understanding, at the atomic scale, the mechanism of oxygen addition and the evolution of the structural and electronic properties step by step. We anticipate that oxidation has a pattern and that electronic properties and reactivity are modified by the charge-density asymmetry induced by incorporating oxygen atoms.

Our manuscript is organized as follows: Section 2 describes the computational details. Section 3 is for the results, and finally, in Section 4, we make the conclusions.

2 Computational details

The oxidation of MoS_2 ($MoSe_2$) to form the MoSO (MoSeO) Janus TMD was investigated *via* quantum mechanical simulations. All calculations were performed in the PWscf code of the Quantum ESPRESSO package.[16–18] A supercell with $3 \times 3 \times 1$ periodicity and a *k*-point density of $3 \times 3 \times 1$ in the first Brillouin zone was used to study the oxidation processes. To avoid interaction between periodic layers along the *z*-axis, a vacuum of 15 Å was used. Electronic states were expanded in plane waves with 60 Ry as the energy cutoff and 480 Ry for the charge-density cutoff. The electron–ion interactions were modeled using ultrasoft pseudopotentials.[19] The exchange–correlation energy was treated according to the generalized gradient approximation with Perdew–Burke–Ernzerhof (PBE) parametrization.[20] The energy convergence threshold was 1×10^{-6} Ry.

Effective band structures and *ab initio* molecular dynamics (AIMD) calculations were performed with the Vienna *Ab initio* Simulation Package (VASP) code.[21] The cutoff energy was set to 450 eV, and the Brillouin zone sampling used the same *k*-point number. To evaluate the O_2 molecule adsorption on the S/Se vacancy models, we included the Grimme-d3 functional to account for long-range interactions.[22] The AIMD calculations were performed to evaluate the structures' thermal stability at 300 K. In the calculations, the Nose–Hoover thermostat[23,24] controls the temperature in combination with an *NVT* ensemble.

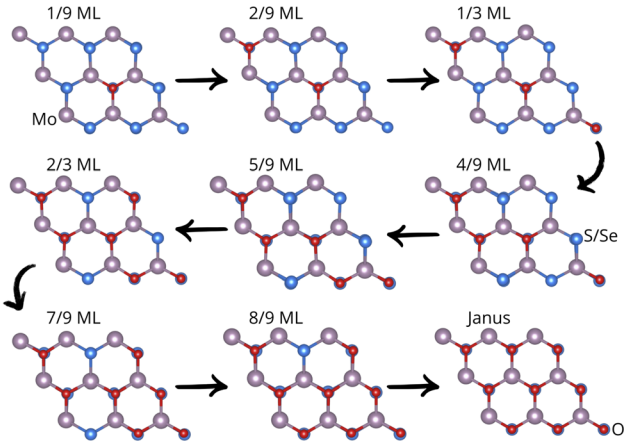

Fig. 1 Oxidation-step snapshots from 1/9 ML to a Janus monolayer. Grey stands for Mo, blue for S/Se, and red for oxygen atoms.

3 Results

First, we describe the atomistic models of the studied structures, MoS_2, $MoSe_2$, MoSO and MoSeO, and determine their lattice parameters. The results are presented in Table 1.

3.1. Oxygen incorporation

In this section, we study the systematic incorporation of oxygen atoms into the pristine monolayers from 1/9 monolayer (ML) to a full ML, see Fig. 1. The oxygen atoms replace S or Se atoms from the same monolayer. We adsorbed O_2 on these systems as a proof of concept to demonstrate its affinity for the S/Se vacancies in MoS_2 and $MoSe_2$. The adsorption energies are -1.89 eV per O_2 and -2.09 eV per O_2 for the S and Se vacancies. These negative energies indicate the viability of forming the Janus material. For structural details, see Fig. S1.† Our results agree with those previously published for O_2 adsorption on sulfur vacancies of MoS_2, in which adsorption energies of around -1.84 eV per O_2 were obtained. Similar results have been reported for $MoSe_2$, with adsorption energies on the selenium vacancy of around -2.15 eV per O_2.[27] The difference in adsorption energies is related to the species' electronegativity. S is more electronegative than Se, so Mo atoms must share more charge with O in $MoSe_2$ than in MoS_2.[27] Structurally, the formed Mo–O bond lengths are 2.17 Å for adsorption on both vacancies and the O–O bond length gets elongated from 1.16 Å in the gas

Table 1 Lattice parameters of pristine and oxidized monolayers. *a* denotes the lattice parameter value calculated in this work, a_{exp} is the experimental value, and a_{teo} is the lattice parameter reported in other works. Meanwhile, d_{M-X} is the distance between the transition metal (M) and chalcogen (X), d_{M-O} is the distance between the M atom and oxygen, finally ∠XMX denotes the angle formed between the arrangement of XMX atoms

Monolayer	$\vec{a}$ (Å)	$\vec{a}_{exp}$ (Å)	$\vec{a}_{teo}$ (Å)	d_{M-X} (Å)	d_{M-O} (Å)	∠XMX (°)
MoS_2	3.19	3.16 (ref. 25)	3.18 (ref. 10)	2.42	—	80.67
$MoSe_2$	3.32	3.28 (ref. 25)	3.31 (ref. 8)	2.54	—	82.64
MoSO	3.00	—	3.00 (ref. 10)	2.40	2.11	74.51
MoSeO	3.07	—	3.07 (ref. 26)	2.51	2.10	77.11

phase to 1.38 Å when adsorbed on a S vacancy of MoS_2 and 1.39 Å when adsorbed on a Se vacancy of $MoSe_2$ (see Fig. S1 in the ESI†). Notice that the O bond elongation facilitates the desorption of the weakly bonded O atom; once desorbed, it can take one other S/Se vacancy to further continue with the oxidation process. Once a full monolayer is incorporated, we reach the Janus structure.

In the next paragraphs, we aim to describe the most probable sites where oxygen atoms are incorporated in each oxidation step by comparing the relative energies (E_r) at each non-equivalent site.

For pristine MoS_2 and $MoSe_2$ monolayers, all sulfur and selenium sites in the $3 \times 3 \times 1$ supercell are equivalent; the first oxygen (1/9 ML O) was incorporated (oxygen takes on a sulfur or selenium site) at the center of the supercell, giving rise to new non-equivalent sites. The second oxygen (2/9 O ML) can be incorporated into the first oxygen's nearest-neighbor sites or far from them, where all sites are equivalent. This systematic search was carried out until a full monolayer was completed, giving rise to the oxidized Janus MoSO and MoSeO phases. Fig. 1 depicts all oxidation steps for both MoS_2 and $MoSe_2$. Our results evidence that oxidation follows a well-defined pattern. First, oxidation proceeds diagonally and then replaces the sulfur ring surrounding the first incorporated oxygen. This way of oxidizing the structure is related to the difference in electronegativity between S(Se) and O atoms and is a way to systematically generate curvature in the 2D systems to increase their reactivity further.

3.2. Oxidation's effect on the lattice parameter

Now, we describe the lattice parameter evolution as the oxygen content increases in MoS_2 and $MoSe_2$ TMDs. The incorporation of each oxygen atom into the S/Se sites at the same monolayer face results in a systematic decrease in the lattice parameter for both MoS_2 and $MoSe_2$ structures; see Fig. 2. We analyzed from 1/9 ML until 1 ML, atom by atom. The lattice parameter contraction is systematic and is related to the difference in atomic radius between the chalcogen species and oxygen atoms, following the order Se > S > O. Notice that the system with Se atoms has the larger lattice parameter followed by the one with S atoms. When reaching the Janus monolayers, the difference in lattice parameter between MoSO and MoSeO is reduced, but it is still larger for MoSeO. Concerning the electronegativities, we have the following order: O > S > Se; this is also a reason for the lattice parameter contraction, since a higher bond order (more attraction between Mo atoms and short bond distances; see Table 1) is expected for the case of oxygen bonded to Mo atoms, driving to a small lattice parameter and larger stability, as discussed in the following section.

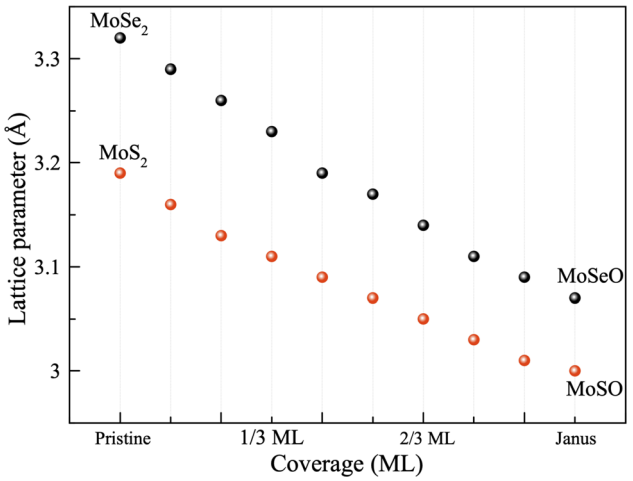

Fig. 2 Oxygen content in MoS_2 and $MoSe_2$ *vs.* lattice parameter (in Å).

3.3. Monolayer stability

This subsection is devoted to studying the stability of MoS_2, $MoSe_2$ and their oxidized counterparts. First, we proceed to study the stability of the oxidized structures under different growth conditions through a thermodynamic stability analysis; after that, we proceed to show their thermal stability by conducting *ab initio* molecular dynamics simulations. The dynamical stability of the oxidized MoSO and MoSeO is not reported since we have already demonstrated that in previous publications.[28,29]

3.3.1. Thermodynamic stability analysis. The relative energy analysis helped us determine in which site the O is located, at different coverages. Still, the relative energy is not useful for describing which coverage is more stable, since it depends on the number of atoms. Instead, the formation energy, which depends on the chemical potentials of the constituent atoms,[30,31] can be used as a tool to describe the stability of different oxygen coverages. The formation energies for each step of oxidation were calculated in accordance with the methodology outlined in the previous references. The complete chemical potential region was then analyzed by varying the oxygen chemical potential from oxygen-rich conditions $\left(\mu_O = \frac{1}{2}\mu_{O_2}\right)$ to oxygen-poor conditions $(\mu_O = -E_{O_2}^{coh})$, where "$E_{O_2}^{coh}$" is the atomization energy of "O_2" molecule. The energy reference in each case is the MoS_2 and $MoSe_2$ monolayers. The E_f can be written as follows:

$$E_f = \frac{E_{M_\alpha X_\beta O_\gamma} - \alpha\mu_{MX_2}^{bulk} + 2(\alpha-\beta)\mu_X - \gamma\mu_O}{\alpha+\beta+\gamma}. \quad (1)$$

where α, β and γ are the number of atoms in the ML with energy $E_{M_\alpha X_\beta O_\gamma}$, $\mu_{MX_2}^{bulk}$ is the chemical potential for the bulk phase of the ML, μ_X is the chemical potential for each element in the most stable phase and μ_O is the chemical potential corresponding to oxygen. Fig. 3a depicts the E_f for $MoS_{2-\gamma}O_\gamma$ at different oxygen contents. In the right part of the figure (O-rich conditions), we can see that the most stable monolayer is Janus MoSO; notice that the stability increases as the number of incorporated oxygen atoms does. From left to right, the first stable structure is the one with one oxygen atom, followed by the one with two, and so on, until reaching a complete monolayer. If we reduce the oxygen chemical potential under intermediate conditions (μ_O from −1.5 to −1.0 eV), several oxygen coverages become stable. For example, at a reduced chemical potential, the most

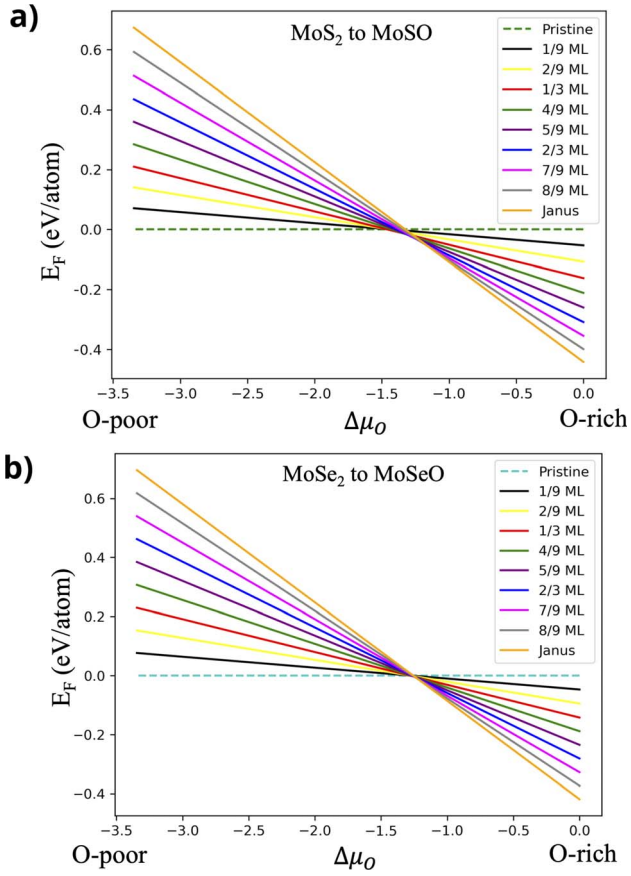

Fig. 3 Formation energies *vs.* oxygen chemical potential, including all oxidation steps. (a) From MoS_2 to MoSO and (b) from $MoSe_2$ to MoSeO.

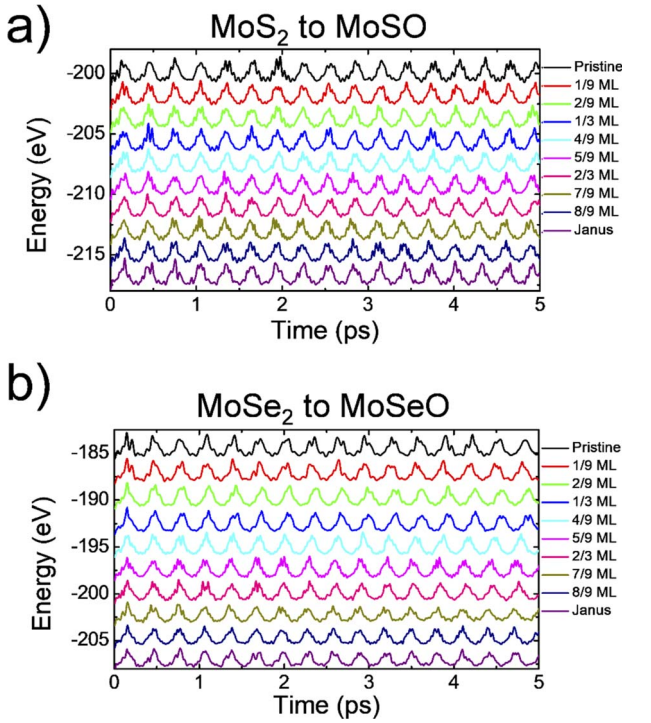

Fig. 4 *Ab initio* molecular dynamics for the intermediate steps between pristine and Janus structures for (a) MoS_2 and (b) $MoSe_2$.

stable oxygen coverage is 8/9 ML; upon reducing the oxygen content, the system stabilizes at 7/9 ML, followed by 2/3 ML, and finally, at 1/3 ML coverage. If μ_O keeps decreasing, we see the pristine structure as the most stable. The thermodynamic analysis shows that keeping oxygen-rich conditions is the best way to reach the Janus monolayer.

A similar behavior is observed in the case of $MoSe_{2-\gamma}O_\gamma$; see Fig. 3b. Under oxygen-rich conditions, the stability follows the same trend as in the MoS_2 case, increasing systematically as oxygen content does. When reducing the μ_O chemical potential from −1.5 to −1.0 eV (intermediate growth conditions), the most stable coverage changes from MoSeO to an oxygen coverage of 8/9 ML, after that to 7/9 ML and 2/3 ML, and finally reaches 1/3 ML. Out of this range, for more O-poor conditions, the most stable structure is the pristine $MoSe_2$. As in the MoS_2 case, the best way to obtain the MoSeO monolayer is by inducing growth in the presence of O-rich conditions.

3.3.2. Thermal stability. The AIMD simulations were carried out for 5 picoseconds (ps) in steps of 5 femtoseconds (fs). The total free-energy fluctuations as a function of time at room temperature are shown in Fig. 4. Fig. 4a shows the results for the different oxygen coverages from pristine MoS_2 to the formation of the Janus MoSO, while Fig. 4b is for the intermediate states from $MoSe_2$ to Janus MoSO. During the simulations, we observe slight movements of the atoms around their equilibrium positions, where no broken Mo–S, Mo–Se, or Mo–O bonds or geometric reconstructions are observed. Our results demonstrate that all systems under study are thermally stable.

3.4. Electronic properties

The semiconducting character of the monolayers has been extensively studied for their pristine phases (MoS_2 and $MoSe_2$), obtaining theoretical values for the direct band gap of 1.62 eV and 1.45 eV, respectively.[32] Also, for the oxidized phases (MoSO and MoSeO), the oxidation of the monolayers has been shown to affect the electronic properties, specifically the band gap, resulting in values of 1.12 eV and 0.83 eV, respectively – going from direct to indirect character, in agreement with previous research (Table 2).[10,26,32] We have undertaken the task of identifying the band-gap evolution at each stable oxidation step for both MoS_2 and $MoSe_2$. Fig. 5 shows coverage *vs.* gap energy for several stable oxidation steps. Notice that there is a clear trend, where the band gap gets reduced as oxygen coverage increases. Notice also that the difference between the band gaps in the

Table 2 Band-gap values in pristine and oxidized monolayers. E_g denotes the band-gap values calculated in this work. E_g^{exp} is the experimental value and E_g^{teo} are the values calculated in other works

Monolayer	E_g (eV)	E_g^{exp} (eV)	E_g^{teo} (eV)	Type
MoS_2	1.62	1.80 (ref. 32)	1.67 (ref. 10)	Direct
$MoSe_2$	1.45	1.50 (ref. 33)	1.58 (ref. 32)	Direct
MoSO	1.12	—	1.07 (ref. 10)	Indirect
MoSeO	0.83	—	0.81 (ref. 26)	Indirect

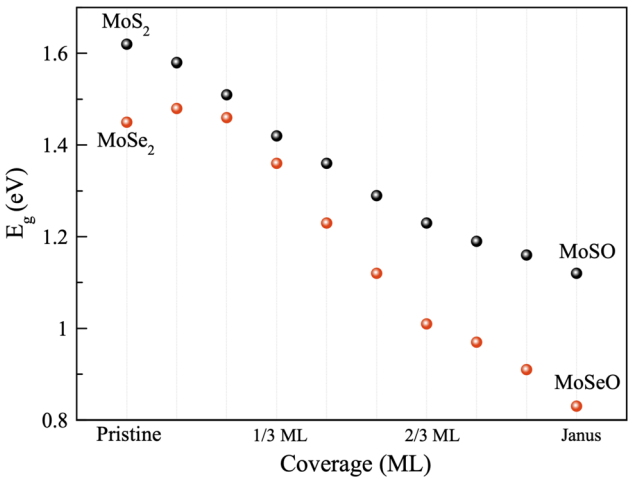

Fig. 5 Variation of band-gap energy for each oxidation process step in both monolayers, from pristine to Janus phases.

pristine structures is 0.17 eV (MoS_2 and $MoSe_2$), which is reduced to 0.06 eV for 1/3 MLs, and then it increases to 0.22 eV for 2/3 MLs. This tendency is maintained until complete oxidation. It further increases as it tends to behave more Janus-like in the 7/9 MLs O, 8/9 MLs, and Janus monolayers. Finally, the gap difference between MoSO and MoSeO is 0.29 eV. The data presented in Fig. 5 evidences a clear band-gap engineering induced by oxidation.

3.4.1. Effective band structures. Band structures are a way to describe much of the physics of materials; they help determine if a material is an insulator, semiconductor, or metal. For semiconductors, bands are used to determine if the transition is direct or indirect. Other interesting properties like effective masses, Fermi velocities, and valley polarization[34] can also be obtained. In this manuscript, we will describe how the bands are modified due to oxidation, mainly determining if the direct (MoS_2) to indirect (MoSO) transition happens at the early stages of oxidation or just when reaching the Janus phase. To elucidate that, and since we are using a supercell, we plotted the effective band structure of all treated coverages to study the band-gap evolution and the coverage at which the direct-to-indirect transition occurs. Electronic states are weighted by occupation; darker dots possess larger weights than lighter ones. The unfolding procedure is based on the one proposed in ref. 35. Notice that the unfolded band structures of the pristine 3×3 MoS_2 and $MoSe_2$ structures resemble the ones reported already in the literature.[36,37] In the case of MoS_2, the direct-to-indirect transition happens just at the first coverage, 1/9 ML O. The indirect transition is retained with a systematic decrease of the band gap, as evident in the upper panels of Fig. 6 and S2.† When we focus on $MoSe_2$, see the lower panels in Fig. 6 and S3,† the band gap increases slightly at the first coverage (1/9 ML O). After that, it systematically decreases until reaching MoSeO. In this case, the direct-to-indirect transition occurs at a coverage of 2/9 ML O. After that, the band gap remains unchanged until reaching MoSeO, a full coverage of oxygen atoms on one side of the $MoSe_2$.

We also calculated the projected density of states (PDOS), presented in the ESI† (Fig. S4 and S5), and the electrostatic potential isosurfaces (EPI), as shown in the next section.

3.4.2. Projected density of states. The PDOS (Fig. S4 and S5†) helps us to describe the contributions of the atoms to the density of states and confirm the semiconductor character of the monolayers in each oxidation step. In our case, the PDOS helps us to determine which types of orbitals are contributing around the Fermi level. We calculated the PDOS for both monolayers at each oxidation stage. As the oxygen concentration increases in one plane of the systems, the sulfur and selenium atoms contribute less with energy states close to the Fermi level. In contrast, the oxygen atoms start to contribute more with electronic states close to the Fermi level.

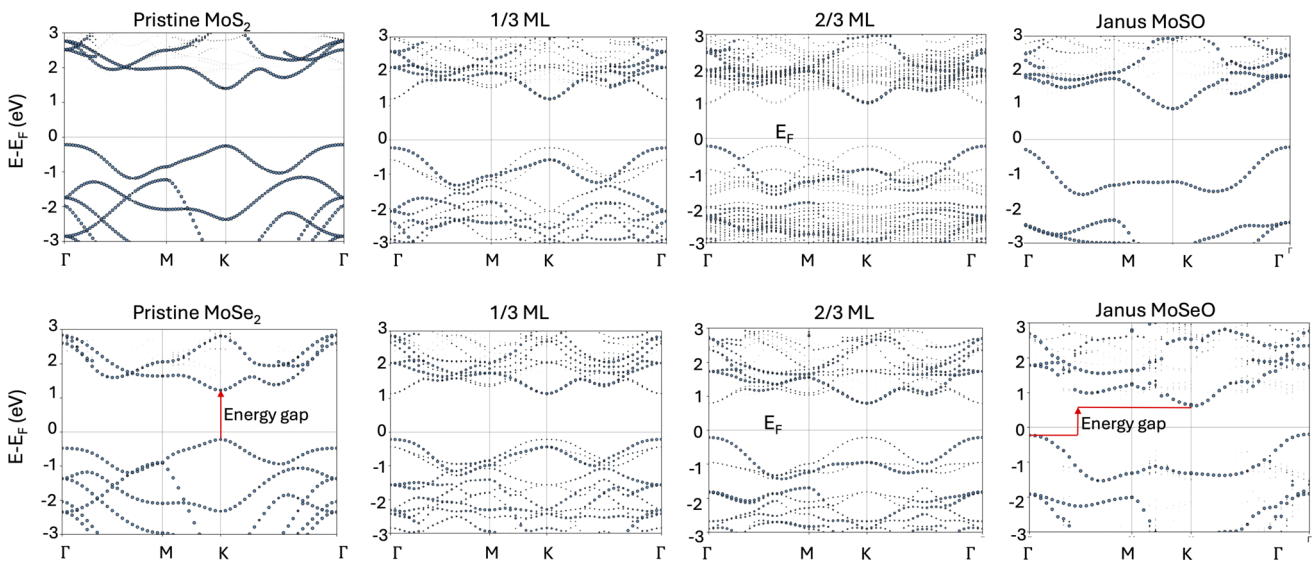

Fig. 6 Effective band structures (unfolded bands) showing oxygen's effect on the band gap at selected oxygen coverages. Zero energy defines the Fermi energy.

Furthermore, in both monolayers, notice that the orbitals that contribute more to the valence band are the d-orbitals of molybdenum and the p-orbitals of oxygen (MoSO and MoSeO). Here, there is an interesting change due to the oxygen substitution by S and Se p-orbitals, which do not contribute close to the Fermi energy, while in the pristine layers, these orbitals were the ones with the largest contributions. This fact is directly related to the difference in electronegativity between O and S or Se, potentially leading to a large reactivity in the oxidized side of the monolayers.

3.4.3. Electrostatic potential isosurface analysis. The electrostatic potential is useful for getting insights into the reactivity of molecules or low-dimensional systems. EPI evidences regions with charge accumulation or depletion. Let's not forget that valence electrons play a very important role in forming bonds between atoms, and, in turn, they will be the electrons most likely to provide the activity and the ones that generate electric current. By convention, red surface regions indicate negative electrostatic potential, green areas define a neutral potential, and blue areas have positive electrostatic potential. In addition, the EPI is a good way to predict what kinds of molecules might interact with the monolayer. Regions with charge depletion (blue regions) are susceptible to interaction with molecules containing regions of high electron density, while regions with charge accumulation (red regions) may interact with molecules containing regions of positive potential.

Fig. 7a and e depict the EPI for the pristine MoS_2 and $MoSe_2$, respectively. In both cases, the Mo atoms show a green color, indicating that these atoms are neutral. Notice also that S zones (Fig. 7a) possess a larger charge accumulation than Se zones (Fig. 7e), an expected behavior since S is more electronegative than Se. Both top and down views of the monolayers are equivalent. Upon incorporating oxygen atoms in the S or Se sites, the system experiences a change in the EPI. In the top view of Fig. 7b and f, at 1/3 ML oxygen coverage, the diagonal turns completely red, meaning that a large charge accumulation is induced by the incorporated oxygen atoms; the remaining zones behave as described before. However, as the oxygen content increases to 7/9 ML (see top views of Fig. 7c and g), the charge accumulation zones increase, and the S or Se monolayer side (down views) is also affected due to the difference in electronegativity, turning more green reddish due to the charge density asymmetry induced by the oxygen atoms. Finally, when reaching the full oxygen coverage (1 ML), the charge density asymmetry is even larger, inducing a clear activity enhancement on the oxygen side, while the S (Fig. 7d) and Se (Fig. 7h) sides are more greenish.

The oxidation of the MoS_2 and $MoSe_2$ monolayers has led us to Janus phases of MoSO and MoSeO, which shows that the oxygen side is very reactive towards oppositely charged molecules (areas of positive electrostatic potential). Therefore, the

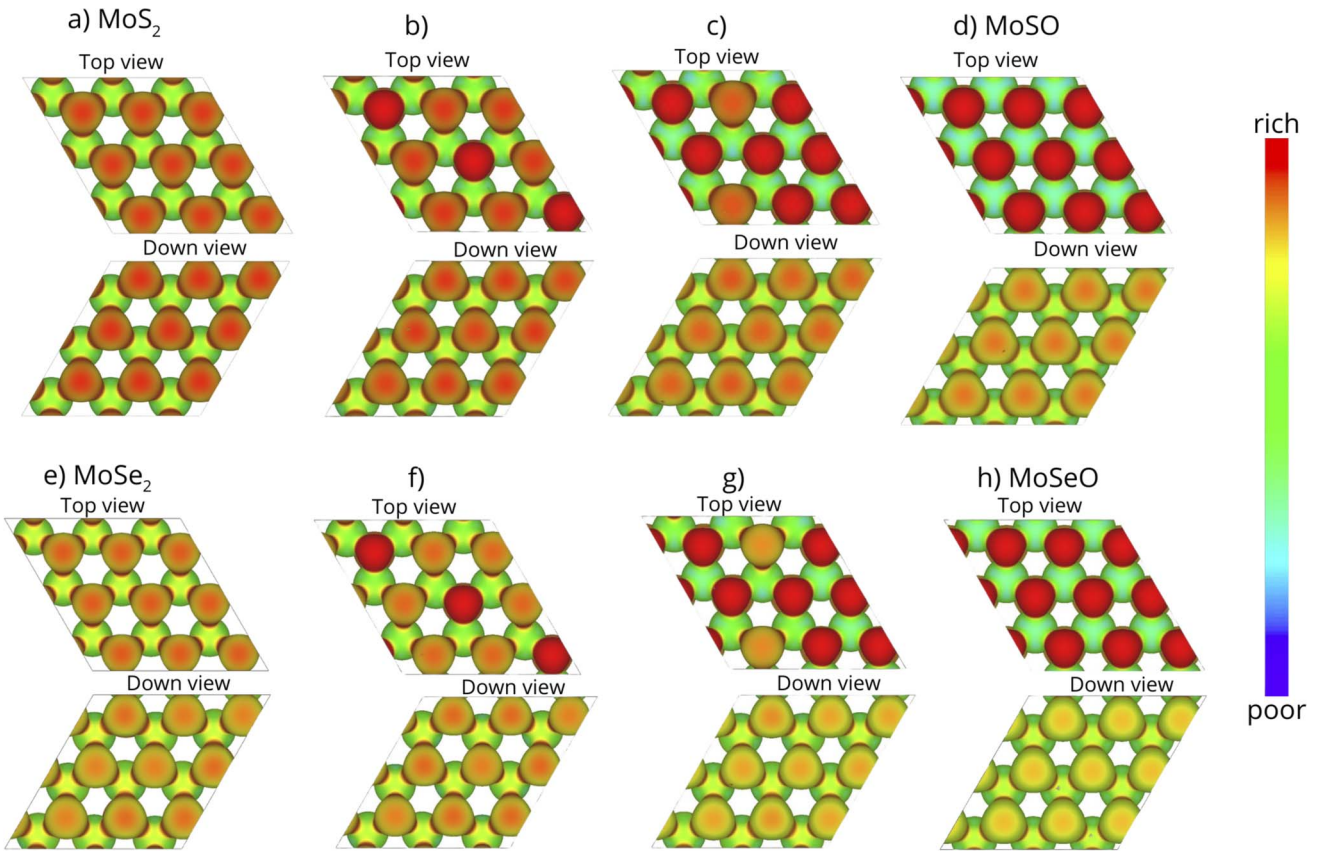

Fig. 7 Electrostatic potential maps of pristine monolayers MoS_2 and $MoSe_2$ (a and e), partially oxidized phases (b, c, f and g), and Janus phases MoSO (d) and MoSeO (h) are presented. Red regions indicate a negative potential value, while blue regions indicate a positive potential value.

oxidized Janus phase has potential applications in molecule traps or gas sensors.

4 Conclusions

In this study, we carried out a systematic analysis of the oxidation of transition metal dichalcogenide monolayers, namely MoS_2 and $MoSe_2$. We identified a pattern in the oxidation of the monolayers on a basal plane; after the incorporation of the first oxygen atom, subsequent oxygen atoms preferentially settled forming diagonal patterns before occupying the remaining positions. The formation energies demonstrated that several oxidized structures stabilize under different growth conditions, but the Janus monolayers (MoSO and MoSeO) are stable under oxygen-rich conditions. The systematic incorporation of oxygen affected the electronic properties, reducing the band gap as the oxygen content increased. The direct-to-indirect band-gap transition happens at the early stages of oxidation. Also, sites where oxygen atoms were incorporated accumulated an excess of negative charge. In contrast, the non-oxidized basal plane tended to have sites with a lower negative charge. The oxygen incorporation increased the reactivity on the O-side due to oxygen's large electronegativity with respect to the chalcogen S and Se atoms. The increase in reactivity induced by oxygen atoms may be used to trap molecules with positive polarities.

Data availability

The data supporting this article is accessible through the corresponding author upon a reasonable request.

Conflicts of interest

There are no conflicts to declare.

Acknowledgements

We thank DGAPA-UNAM projects IG101124, IA100624, and IN101523 for their financial support. Calculations were performed in the DGCTIC-UNAM Supercomputing Center, project no. LANCAD-UNAM-DGTIC-150, LANCAD-UNAM-DGTIC-368 and LANCAD-UNAM-DGTIC-422. We thank Aldo Rodriguez-Guerrero for their technical support and useful discussions.

References

1 A. Geim and K. Novoselov, The rise of graphene, *Nat. Mater.*, 2007, **6**, 183–191, DOI: **10.1038/nmat1849**.

2 A. Kokabi, M. Bahramy and S. Babaee Touski, Spin and electronic property prediction of IV–V binary monolayers using deep knowledge transfer method, *J. Magn. Magn. Mater.*, 2024, **590**, 171602, DOI: **10.1016/j.jmmm.2023.171602**.

3 S. Manzeli, D. Ovchinnikov, D. Pasquier, V. Yazyev and K. Andras, 2D transition metal dichalcogenides, *Nat. Rev. Mater.*, 2017, **2**, 17033, DOI: **10.1038/natrevmats.2017.33**.

4 S. E. Kadantsev and P. Hawrylak, Electronic structure of a single MoS_2 monolayer, *Solid State Commun.*, 2012, **152**, 909–913, DOI: **10.1016/j.ssc.2012.02.005**.

5 A. Nourbakhsh, A. Zubair, R. N. Sajjad, K. G. A. Tavakkoli, W. Chen, S. Fang, X. Ling, J. Kong, M. S. Dresselhaus, E. Kaxiras, K. K. Berggren, D. Antoniadis and T. Palacios, MoS_2 Field-Effect Transistor with Sub-10 nm Channel Length, *Nano Lett.*, 2016, **16**, 7798–7806, DOI: **10.1021/acs.nanolett.6b03999**.

6 A. K. Singh, P. Kumar, D. J. Late, A. Kumar, S. Patel and J. Singh, 2D layered transition metal dichalcogenides (MoS_2): Synthesis, applications and theoretical aspects, *Appl. Mater. Today*, 2018, **13**, 242–270, DOI: **10.1016/j.apmt.2018.09.003**.

7 B. Radisavljevic, A. Radenovic, J. Brivio, V. Giacometti and A. Kis, Single-layer MoS_2 transistors, *Nat. Nanotechnol.*, 2011, **6**, 147–150, DOI: **10.1038/nnano.2010.279**.

8 L. Hongsheng, H. Nannan and Z. Jijun, Atomistic insight into the oxidation of monolayer transition metal dichalcogenides: from structures to electronic properties, *RSC Adv.*, 2015, **5**, 17572–17581, DOI: **10.1039/C4RA17320A**.

9 J. Paez, R. Ponce, H. Fernández, D. Hoat, E. Murillo, M. Moreno, D. Galván and J. Guerrero, The effect of shape and size in the stability of triangular Janus MoSSe quantum dots, *Sci. Rep.*, 2021, **11**, 21061, DOI: **10.1038/s41598-021-00287-6**.

10 T. Wang, M. Su, H. Jin, J. Li, L. Wan and Y. Wei, Optical, Electronic, and Contact Properties of Janus-MoSO/MoS_2 Heterojunction, *J. Phys. Chem. C*, 2020, **124**, 15988–15994, DOI: **10.1021/acs.jpcc.0c04042**.

11 A.-Y. Lu, H. Zhu, J. Xiao, C.-P. Chu, Y. Han, M.-G. Chiu, C.-C. Cheng, C.-W. Yang, K.-H. Wei, Y. Yang, Y. Wang, D. Sokaras, D. Nordlund, P. Yang, A. D. Muller, M.-Y. Chou, X. Zhang and L.-J. Li, Janus monolayers of transition metal dichalcogenides, *Nat. Nanotechnol.*, 2017, **12**, 744–749, DOI: **10.1038/nnano.2017.100**.

12 M. Yagmurcukardes and F. M. Peeters, Stable single layer of Janus MoSO: Strong out-of-plane piezoelectricity, *Phys. Rev. B*, 2020, **101**, 155205, DOI: **10.1103/PhysRevB.101.155205**.

13 M. H. Rahman, E. H. Haque and S. Hong, High temperature oxidation of monolayer MoS_2 and its effect on mechanical properties: A ReaxFF molecular dynamics study, *Surf. Interfaces*, 2021, **26**, 101371, DOI: **10.1016/j.surfin.2021.101371**.

14 H. S. Waheed, H. Ullah, M. W. Iqbal and Y. H. Shin, Optoelectronic and photocatalytic properties of Mo-based Janus monolayers for solar cell applications, *Optik*, 2022, **271**, 170071, DOI: **10.1016/j.ijleo.2022.170071**.

15 H. S. Waheed, M. Asghar, H. S. Ahmad, T. Abbas, H. Ullah, R. Ali, M. J. Iqbal Khan, M. W. Iqbal, Y.-H. Shin, M. Sheraz Khan and R. Neffatim, Janus MoSO and MoSSe Monolayers: A Promising Material for Solar Cells and Photocatalytic Applications, *Phys. Status Solidi B*, 2023, **260**, 2200267, DOI: **10.1002/pssb.202200267**.

16 P. Giannozzi, S. Baroni, N. Bonini, M. Calandra, R. Car, C. Cavazzoni, D. Ceresoli, G. L. Chiarotti, M. Cococcioni, I. Dabo, A. Dal Corso, S. de Gironcoli, S. Fabris, G. Fratesi,

R. Gebauer, U. Gerstmann, C. Gougoussis, A. Kokalj, M. Lazzeri, L. Martin-Samos, N. Marzari, F. Mauri, R. Mazzarello, S. Paolini, A. Pasquarello, L. Paulatto, C. Sbraccia, S. Scandolo, G. Sclauzero, A. P. Seitsonen, A. Smogunov, P. Umari and R. M. Wentzcovitch, QUANTUM ESPRESSO: a modular and open-source software project for quantum simulations of materials, *J. Phys.: Condens. Matter*, 2009, **21**, 395502, DOI: 10.1088/0953-8984/21/39/395502.

17 P. Giannozzi, O. Andreussi, T. Brumme, O. Bunau, M. Buongiorno, M. Calandra, R. Car, C. Cavazzoni, D. Ceresoli, M. Cococcioni, N. Colonna, I. Carnimeo, A. Dal Corso, S. Gironcoli, P. Delugas, J. DiStasio, A. Ferretti, A. Floris, G. Fratesi, G. Fugallo, R. Gebauer, U. Gerstmann, F. Giustino, T. Gorni, J. Jia, M. Kawamura, H. Y. Ko, A. Kokalj, E. Küçükbenli, M. Lazzeri, M. Marsili, N. Marzari, F. Mauri, N. Nguyen N, H. Nguyen, A. Otero-de-la-Roza, L. Paulatto, S. Poncé, D. Rocca, R. Sabatini, B. Santra, M. Schlipf, A. Seitsonen, A. Smogunov, I. Timrov, T. Thonhauser, P. Umari, N. Vast, X. Wu and S. Baroni, Advanced capabilities for materials modelling with Quantum ESPRESSO, *J. Phys.: Condens.Matter*, 2017, **29**, 465901, DOI: 10.1088/1361-648X/aa8f79.

18 P. Giannozzi, O. Baseggio, P. Bonfà, D. Brunato, R. Car, I. Carnimeo, C. Cavazzoni, S. Gironcoli, P. Delugas, F. Ferrari Ruffino, A. Ferretti, N. Marzari, I. Timrov, A. Urru and S. Baroni, Quantum ESPRESSO toward the exascale, *J. Chem. Phys.*, 2020, **152**, 154105, DOI: 10.1063/5.0005082.

19 A. Dal Corso, Pseudopotentials periodic table: From H to Pu, *Comput. Mater. Sci.*, 2014, **95**, 337–350, DOI: 10.1016/j.commatsci.2014.07.043.

20 J. Perdew, K. Burke and M. Ernzerhof, Generalized Gradient Approximation Made Simple, *Phys. Rev. Lett.*, 1996, **77**, 3865–3868, DOI: 10.1103/PhysRevLett.77.3865.

21 G. Kresse and J. Hafner, Ab initiomolecular dynamics for liquid metals, *Phys. Rev. B: Condens. Matter Mater. Phys.*, 1993, **47**(1), 558–561, DOI: 10.1103/physrevb.47.558.

22 S. Grimme, J. Antony, S. Ehrlich and H. Krieg, A consistent and accurateab initioparametrization of density functional dispersion correction (DFT-D) for the 94 elements H-Pu, *J. Chem. Phys.*, 2010, **132**(15), 154104, DOI: 10.1063/1.3382344.

23 S. Nosé, A unified formulation of the constant temperature molecular dynamics methods, *J. Chem. Phys.*, 1984, **81**, 511–519, DOI: 10.1063/1.447334.

24 W. G. Hoover, Canonical dynamics: Equilibrium phase-space distributions, *Phys. Rev. A*, 1985, **31**, 1695, DOI: 10.1103/PhysRevA.31.1695.

25 J. A. Wilson and A. D. Yoffe, The transition metal dichalcogenides discussion and interpretation of the observed optical, electrical and structural properties, *Adv. Phys.*, 2006, **18**, 193–335, DOI: 10.1080/00018736900101307.

26 V. Van On, D. Khanh Nguyen, J. Guerrero-Sanchez and D. M. Hoat, Exploring the electronic band gap of Janus MoSeO and WSeO monolayers and their heterostructures, *New J. Chem.*, 2021, **45**, 20776–20786, DOI: 10.1039/D1NJ04427C.

27 H. Liu, N. Han and J. Zhao, Atomistic insight into the oxidation of monolayer transition metal dichalcogenides: from structures to electronic properties, *RSC Adv.*, 2015, **5**, 17572–17581, DOI: 10.1039/C4RA17320A.

28 D. K. Nguyen, J. Guerrero-Sanchez, V. Van On, J. F. Rivas-Silva, R. Ponce-Pérez, G. H. Cocoletzi and D. M. Hoat, Tuning MoSO monolayer properties for optoelectronic and spintronic applications: effect of external strain, vacancies and doping, *RSC Adv.*, 2021, **11**(56), 35614–35623, DOI: 10.1039/D1RA05639E.

29 V. Van On, D. K. Nguyen, J. Guerrero-Sanchez and D. M. Hoat, Exploring the electronic band gap of Janus MoSeO and WSeO monolayers and their heterostructures, *New J. Chem.*, 2021, **45**(44), 20776–20786, DOI: 10.1039/D1NJ04427C.

30 M. Hillert, The compound energy formalism, *J. Alloys Compd.*, 2001, **320**, 161–176, DOI: 10.1016/S0925-8388(00)01481-X.

31 Q. Guo-Xin, M. Martin and D. Chadi, *Phys. Rev. B: Condens. Matter Mater. Phys.*, 1988, **38**, 7649, DOI: 10.1103/PhysRevB.38.7649.

32 A. Kumar and P. K. Ahluwalia, Electronic structure of transition metal dichalcogenides monolayers 1H-MX_2 (M = Mo, W; X = S, Se, Te) from ab-initio theory: new direct band gap semiconductors, *Eur. Phys. J. B*, 2012, **85**, 186, DOI: 10.1140/epjb/e2012-30070-x.

33 X. Wang, Y. Gong, G. Shi, W. Leong, K. Keyshar, G. Ye, R. Vajtai, J. Lou, Z. Liu, E. Ringe, B. Kang and M. Pulickel, Chemical Vapor Deposition Growth of Crystalline Monolayer $MoSe_2$, *ACS Nano*, 2014, **8**, 5125–5131, DOI: 10.1021/nn501175k.

34 A. Xie, H. Hao, C.-S. Liu, X. Zheng, L. Zhang and Z. Zeng, Giant tunnel electroresistance in two-dimensional ferroelectric tunnel junctions constructed with a Sc_2CO_2/In_2Se_3 van der Waals ferroelectric heterostructure, *Phys. Rev. B*, 2023, **107**(11), 115427, DOI: 10.1103/physrevb.107.115427.

35 V. Popescu and A. Zunger, Effective Band Structure of Random Alloys, *Phys. Rev. Lett.*, 2010, **104**(23), 236403, DOI: 10.1103/physrevlett.104.236403.

36 J. You, Y.-S. Kim, K. C. Santosh and K. Cho, Monolayer MoS_2 Bandgap Modulation by Dielectric Environments and Tunable Bandgap Transistors, *Sci. Rep.*, 2016, **6**, 29184, DOI: 10.1038/srep29184.

37 S. K. Pandey, R. Das and P. Mahadevan, Layer-Dependent Electronic Structure Changes in Transition Metal Dichalcogenides: The Microscopic Origin, *ACS Omega*, 2020, **5**, 15169–15176, DOI: 10.1021/acsomega.0c01138.